Membrane potential as master regulator of cellular mechano-transduction

Avik Mukherjee*, Yanqing Huang*, Jens Elgeti, Seungeun Oh, Jose Abreu, Anjali Rebecca Neliat, Janik Schüttler, Dan-Dan Su, Christoph Dupre, Nina Catherine Benites, Xili Liu, Leonid Peshkin, Mihail Barboiu, Hugo Stocker, Marc W. Kirschner, Markus Basan[#]

[#] Correspondence: markus@hms.harvard.edu , *equal contribution

The establishment of membrane potential is a property of all living cells[1]. Nevertheless, its physiological role in non-excitable cells is poorly understood. Resting membrane potential is typically considered fixed for a given cell type and under tight homeostatic control[2]. Contrary to this paradigm, we find that membrane potential is a dynamic property that directly reflects mechanical forces acting on the cell. Cells use membrane potential to assess their biomechanical state and we show that important mechano-sensitive signaling pathways, like MAPK and Hippo[3–8], are directly controlled by membrane potential via upstream membrane-bound receptors, such as Fat1. We further show that mechano-transduction via membrane potential plays a critical role in the homeostasis of epithelial tissues, setting cellular biomass density and cell number density by controlling proliferation and cell elimination. In epithelial scratch wound assays and *Xenopus* tadpole tail regeneration, we observe a wave of depolarization, resulting from a drop in cellular biomass density due to mechanical stretch. This depolarization wave enhances the efficiency of wound closure. Together, these data are explained by a biophysical model that demonstrates that membrane potential is physically coupled to mechanical pressure and cellular biomass density, thereby providing a quasi-instantaneous, global readout of the biophysical state of the cell. Membrane potential in turn regulates cell growth, resulting in homeostatic feedback control of biomass density and cell number density in tissues. This may be an ancient mechanism for growth control in multi-cellular organisms and its misregulation may play a role in tumorigenesis.

How the volume, mass and macromolecule density of metazoan cells are regulated is yet to be fully understood but critical for biochemical functions at cellular level, as well as for the growth and homeostasis of tissues and organisms. It is typically assumed that biomass density is constant, indicating that cell mass and volume are directly proportional. However, this assumption has not been thoroughly tested experimentally.

Quantification of tissue biomass density

We grew different cell lines that model epithelial monolayers of varying tissue origin[9], including Madin Darby Canine Kidney (MDCK), MCF10a, and EpH4-Ev. We used normalized Raman imaging (NoRI)[10] to quantify intracellular biomass densities at increasing levels of confluence. Remarkably, rather than remaining constant, in all cases, cellular biomass density underwent a striking increase as a function of cell number density. Fig. 1a shows the nuclei density and biomass density of MDCK cells 0 hours, 48 hours, and 96 hours after initially reaching confluence, and Fig. S1a-d shows the separate protein and lipid contributions. We observed a similar trend in MCF10a and EpH4-Ev monolayers (Fig. 1c, 1d, Fig. S1e, S1f). We confirmed this observation with a second independent microscopic technique, based on laser interferometry, also referred to as holo-tomographic microscopy (Tomocube) (Fig. 1a, red squares & Fig. S3)[11,12].

Tissue density is reflected in membrane potential

Inspired by physical phenomena from equilibrium thermodynamics[13], we wanted to know whether changes in biomass density were reflected in changes of membrane potential. Using the hybrid voltage-indicator Voltron[14], we quantified the membrane potential in MDCK cells as a function of cell number and biomass density. Strikingly, MDCK cells became increasingly hyperpolarized with increasing cell number (Fig. 1b). In MCF10a and EpH4-Ev cells, we also confirmed the hyperpolarization of membrane potential with increasing cell number density (Fig. 1c and Fig. 1d lower panel) with the membrane potential dye $DiOC_2(3)$. These findings are consistent with previous glass-microelectrode based measurements of resting membrane potential in CHO cells as they reached different levels of confluence over time (Fig. S4a, and S4b) and in different regions of the colony with varying local density[15](Fig. S4d). Similarly, our measurements in different regions of CHO colonies showed increasing depolarization with decreasing cell number density (such as colony edge), whereas denser regions of the colony exhibit hyperpolarized membrane potential (Fig. S3e). The mechanistic basis or consequence of these early observations has never been explained. We hypothesized that, just like in MDCK cells, changes in CHO cells' membrane potential might correlate with changes in cellular biomass density. Indeed, using NoRI imaging, we confirmed that in CHO cells also progressively get denser in biomass density with increasing confluence (Fig. S4c). Unlike MDCK or MCF10a cells, CHO cells do not form a tight epithelium connected by tight junctions, suggesting the relationship between membrane potential and biomass density is general.

The correlation of biomass density and membrane potential suggests that these physiological variables are directly coupled. To test the causal nature of this relationship, we applied external osmotic pressure to compress cells, artificially increasing their biomass density, and found that the membrane potential of both cell lines hyperpolarized (Fig. S5). Therefore, changes in membrane potential may be a direct result of changes in biomass density.

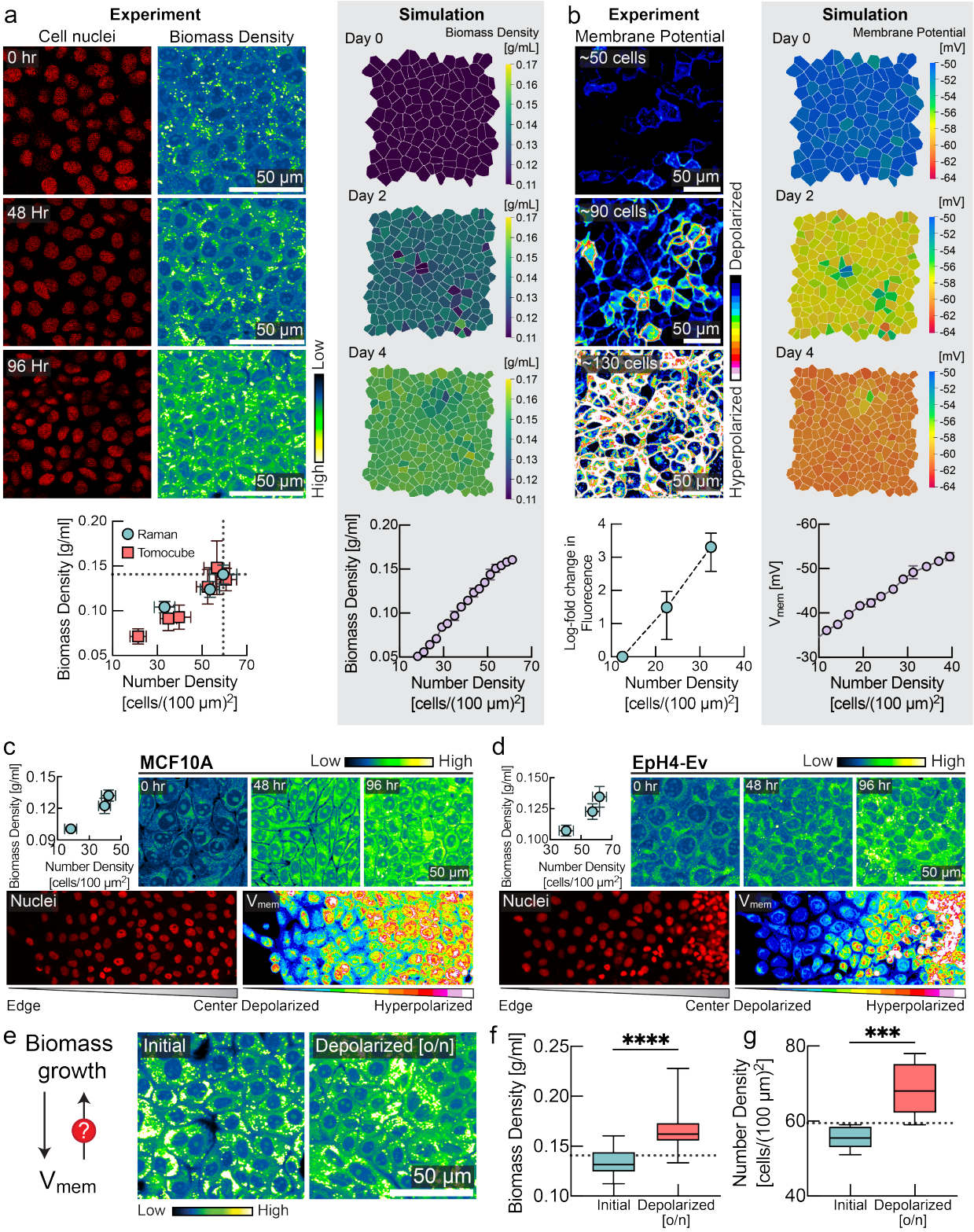

Figure 1: Membrane potential is a sensor and regulator of tissue density. a*, MDCK cells imaged for 4 consecutive days after confluence with increasing cell number density. Left panel shows number of cell nuclei and cellular biomass density (in units of g/ml) measured via Normalized*

Stimulated Raman Spectroscopy (NoRI). Plot below shows correlation between number density (mean ± s.d., NoRI: n=8, Tomocube: n=10) and biomass density (mean ± s.d., NoRI: n=15, Tomocube: n=~20) measured using NoRI and Tomocube. Right panel displays snapshots of biomass density in tissue simulation (mean ± s.d., n=4 simulations). ***b,*** *Left panel shows fluorescence of MDCK-Voltron cells, plot below shows log fold change in fluorescence (mean ± s.d., n=8) against number density. Right panel displays snapshots of membrane potential in tissue simulation (mean ± s.e.m., n=4 simulations).* ***c-d****, Top panels: NoRI images and quantification (mean ± s.d., number density: n=~10, NoRI: n=24) of MCF10A/EpH4-Ev cells for 4 consecutive days after confluence with increasing cell number density. Bottom panels: $DiOC_2(3)$ imaging from colony edge to colony centre.* ***e****. Feedback control loop between biomass growth and membrane potential is crucial for epithelial homeostasis.* ***f-g****, Depolarization of membrane potential by ouabain increases the biomass density (box plot, line at mean, error bars represent min to max, n=40) and number density (n = 8) of confluent cells over the homeostatic steady state limit (dotted line; quantified from experiment in panel a).*

Membrane potential regulates biomass density and cell number density

Based on these observations, we hypothesized that membrane potential could be directly involved in regulating biomass density of cells in a tissue and cell number density. To test this hypothesis, we first grew MDCK monolayer to its optimum homeostatic density (Fig. 1e) and confirmed that cells reached homeostatic biomass density threshold by NoRI (Fig. 1e, 1f). After this, we depolarized the cells by inhibiting the sodium-potassium pump (using pharmacological inhibitor ouabain) and observed that depolarization pushed cells to go over the homeostatic limit of biomass density (Fig 1e,f), as well as number density (Fig. 1g). We also confirmed this phenotype is independent of ways by which depolarization is induced in a more high-throughput experiment. We grew MDCK cells to maximum density and then applied either depolarizing (gramicidin, TCT[16,17]) or hyperpolarizing (valinomycin) drugs at different concentrations to the tissue culture. Cells in depolarizing conditions (Fig. S6a, red) maintained a significantly higher cell number density than cells grown in the absence of drugs (Fig. S6a, cyan). Conversely, the cell number density in hyperpolarizing conditions (Fig. S6a, yellow) dropped and then plateaued at a substantially lower level than WT. This steady-state cell number density could be modulated continuously with the dose of the hyperpolarizing drug (Fig. S6c), consistent with a regulatory role of membrane potential in controlling tissue density.

Mechano-electro-osmotic model

To understand how membrane potential might control biomass density and the effect of cell number density on proliferation, we created a biophysical mathematical model of ion homeostasis, cellular biomass and mechanical pressure. Classical models of membrane potential do not consider mechanical forces at all, and their systems of equations are only closed by introducing unphysical simplifications[2,18]. Models correctly rooted in elementary physical laws were developed in the 1960s and showed that osmotic stabilization of cells requires constant ion export that results in a build-up of membrane potential as a by-product[19–21]. However, it remained unclear how these models should be applied to growing cells, as they change in cell mass, cell membrane and volume, and model parameters like permeability and transport activity are subject to change. More importantly, none of these works uncovered that membrane potential, a by-product of volume stabilization, may directly convey crucial physiological information to cells and direct cellular decision making.

Membrane potential is in fact intimately coupled to osmotic pressure of the cytoplasm and the balance of charged ions and macromolecules inside the cell. As illustrated in Box 1 (top), an imaginary cell resists external forces compressing it via osmotic pressure resulting from an increased concentration of intracellular macromolecules in the cytoplasm and an increased concentration of counterions. However, this results in a steeper ion concentration gradient across the plasma membrane promoting a larger efflux of ions. A buildup of membrane potential due to charged biomolecules inside the cell counteracts this diffusive efflux, retaining an elevated intracellular ion concentration to counteract the external pressure. In equilibrium conditions, this is known as the Gibbs-Donnan effect[13], but the same processes are at play far from equilibrium. With a constant expression ratio of ion transporters and channels, membrane potential constitutes a cell size-independent readout of total mechanical pressure on the cell and the corresponding cytoplasmic biomass density (see Box 1 & Supplementary Note 1). In effect, membrane potential physically controls biomass density and mechanical forces, and vice versa, but crucially it provides cells with an accessible readout of biomass density and mechanical forces for signal transduction. Of note, the polarity of the membrane potential in the model is determined by the net charge on the macromolecules in the cell. Negative charge dominates over positive because the proteome has an average isolectric point above 7[22] and nucleic acids, especially the significant fraction of the biomass in the cytoplasm comprised of RNA[23], are negatively charged. As a result, K+ and Na+ are the abundant cations in the cytoplasm, and the membrane potential polarity is such that there is net negative charge on the inside of the cell.

Tissue simulation

We calibrated the mechano-electro-osmotic model with physiological parameters and use it to simulate a mono-layered epithelium (Supplementary Note 2). Membrane potential provides cells in the tissue with a quasi-instantaneous readout of tissue density and the mechanical constraints, which are important for tissue homeostasis (Fig. 1c). Because the coupling between mechanics, density, and membrane potential requires no active regulation and is present even at thermodynamic equilibrium, we hypothesize that regulation via membrane potential could be one of the earliest homeostatic mechanisms employed in multi–cellular organisms. To test the idea that tissues can achieve homeostasis relying only on the membrane potential as a controller, we tested a model where the membrane potential is the sole regulator of biosynthesis and apoptosis (see Supplementary Note 2 for details of implementation).

Indeed, the tissue simulation successfully recapitulated our experimental observations, including the increase in biomass density with cell number density (Fig. 1a, right side) and the corresponding changes in membrane potential (Fig. 1b, right side). Implementing the mechanism of different depolarizing and hyperpolarizing drugs in the simulation, the model recapitulated the observed changes in steady-state tissue density (Fig. S6b). The general effect of these drugs can be understood intuitively: cells perceive mild depolarization to be a state of low confluence. They continue to grow generating an excessive density (Fig. S6b, red circles). Conversely, hyperpolarization by drugs leads to a lower homeostatic tissue density because cells seem to interpret hyperpolarization as excess tissue density and arrest their growth prematurely (Fig. S6b, yellow circles). The regulation of cell growth by membrane potential correctly predicts changes in steady-state tissue density.

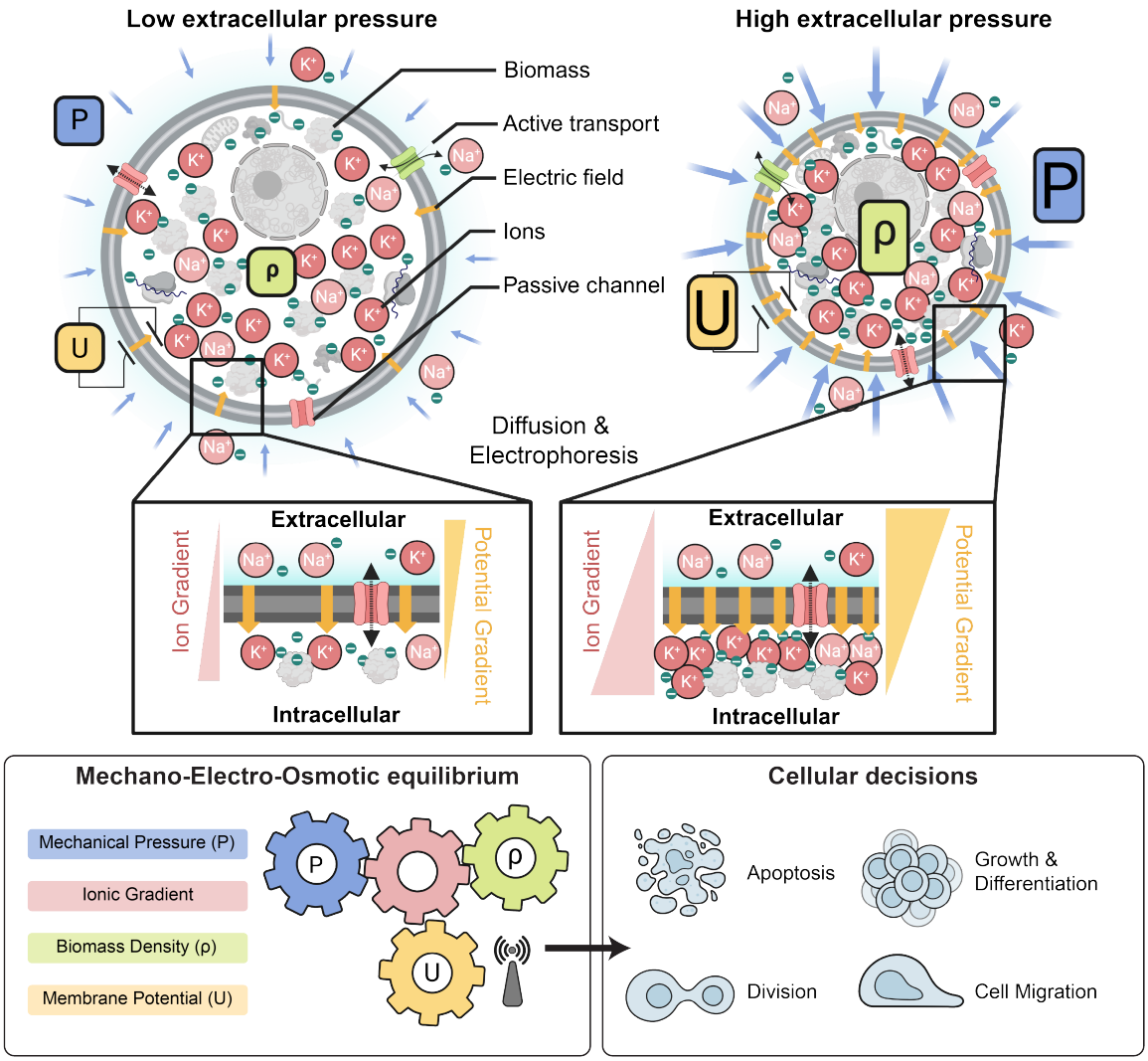

Box 1: Mechano-electro-osmotic model. Top: *The model combines three elementary conservation laws: Flux balance across the plasma membrane, mechanical force balance, and charge balance. Left-hand side illustrates a cell under low mechanical pressure and the right-hand side a corresponding cell under high mechanical pressure. Cellular biomass like protein and RNA carries a net negative charge. Cells resist compression of their volume via cytoplasmic osmotic pressure that counteracts and balances external forces (force balance). This osmotic pressure originates from an intracellular concentration of counterions that are attracted to balance negatively charged macromolecules (charge balance). As illustrated on the right-hand side, higher mechanical pressure acting in the cell is thus balanced by a higher concentration of counterions. Higher intracellular ion concentrations result in steeper concentration gradients across the membrane, as illustrated in the right inset. With constant ion channel abundances, a steeper concentration gradient across the membrane results in an augmented diffusive efflux of ions (Fick's law). With constant active ion transport flux (sodium-potassium-ATPase), this increased diffusive ion efflux results in a buildup of net negative charge in the cytoplasm and a corresponding membrane potential that counteracts the diffusive efflux of positively charged ions until flux*

balance is achieved (flux balance for each ion species). ***Bottom:*** *A one-to-one correspondence between mechanical pressure, cytoplasmic biomass density and membrane potential emerges from the mechano-electro-osmotic equilibrium illustrated in the top panel. Crucial physiological properties like total biomass in relation to available space or mechanical and spatial constraints on the entire cell are difficult for cells to assess and integrate from individual molecular players. Membrane potential, on the other hand, provides an instantaneous, global readout of these physiological variables. We hypothesize that membrane potential is therefore the ideal starting point for signal transduction to control cellular decisions like growth, apoptosis, and cell motility to achieve tissue homeostasis.*

Membrane potential reflects mechanical forces

The mechano-electro-osmotic model (Box 1) predicts that mechanical forces should be directly reflected in the membrane potential. To test this prediction, we imposed external mechanical perturbations on the tissue and measured the response of membrane potential. One method is to culture epithelial cells on an elastic membrane that can be stretched or de-stretched mechanically, thereby expanding or compressing the tissue itself[24,25] (Fig. 2a). We cultured MDCK cells on a stretchable PDMS membrane and waited until cells reached maximum cell number density. We employed the voltage sensitive dye FluoVolt, whose fluorescence intensity increases with depolarization[26], as it is ideally suited to image changes in membrane potential on short timescales. Indeed, stretching the MDCK monolayer resulted in depolarization (Fig. 2a,b, quantified in panel c), consistent with simulation prediction (Fig. 2d). To check that this change in membrane potential was reversible on short timescales when we de-stretched the membrane, we used a different voltage indicator,$DiSBAC_2(3)$[27], which is more reversible than FluoVolt in short timescales. As predicted in the model (Fig. 2g), reducing the stretch of the PDMS membrane quickly led to repolarization of membrane potential (Fig. 2e,f). According to the model, depolarization upon stretch is caused by a drop in cellular biomass density due to an increased cell volume, rather than tension in the plasma membrane or changes in cell-cell adhesion. Using NoRI imaging, we quantified biomass density of the confluent monolayer just before and immediately after a 20% uniaxial stretch, and then again after overnight cultivation (Fig. 2h,i). As expected from the tissue simulation (Fig. 2j), we found that stretching resulted in a significant drop in biomass density and induced biomass production and proliferation, as biomass density and cell number recovered to their initial level overnight. Conversely, we also confirmed that destretching the PDMS membrane resulted in an increase of cellular biomass density after overnight recovery (Fig. S7).

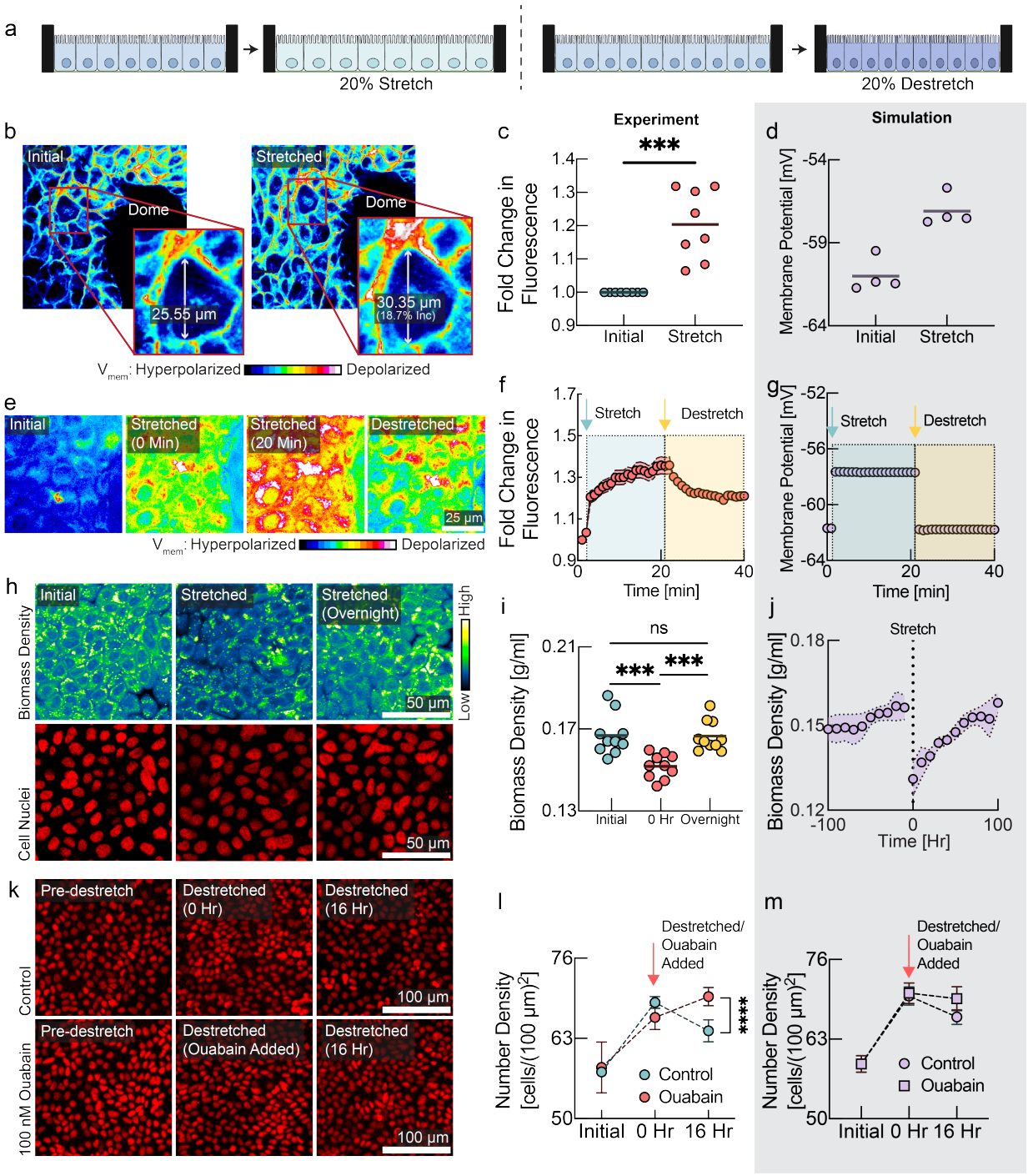

Figure 2: Cells detect and respond to mechanical forces via membrane potential. a, *Schematic diagram depicting the experimental design with monolayers grown on stretchable membrane. In one case, cells were grown to confluence and then 20% uniaxial stretch was applied (left panel) or cells were grown to confluence on a pre-stretched membrane, and then the stretch was released to induce compression (right panel).* ***b,*** *FluoVolt images of MDCK cells before and after stretching.* ***c,*** *Quantification of panel b (line at mean, n=8, p=0.0006, paired t-test).* ***d,*** *Membrane potential predicted by the tissue simulation upon a 20% uniaxial stretch (line at mean, n=4*

simulations, each point is averaged across all cells in simulation). ***e,*** *$DiSBAC_2(3)$ imaging of MDCK cells before stretching, during stretching, and after destretching showing the reversibility of membrane potential change.* ***f,*** *Quantification of panel e (mean ± s.d., n = 8). Increase in fluorescence intensity indicates depolarization and decrease indicates hyperpolarization. Time of stretch and destretch are indicated by cyan and yellow arrows respectively.* ***g,*** *Membrane potential predicted by the tissue simulation upon stretch and subsequent destretch (n=4 simulations, each point is averaged across all cells in simulation).* ***h****, NoRI images of cellular biomass in response to tissue stretch. Biomass density recovers to the initial biomass density level overnight.* ***i,*** *Quantification of panel h. 0 hr represents time of stretch. (n=10, p-values: 0.0006 (initial vs 0 hr), 0.0001 (0 hr vs overnight), unpaired t test).* ***j,*** *Tissue simulation recapitulates the drop of biomass density upon stretch and overnight recovery. (mean ± s.d., n=4 simulations)* ***k,*** *Rescue of destretching-induced tissue crowding by ouabain. After 16 hr, a significant number of cells had been eliminated, consistent with previous studies[24,25].* ***l,*** *Quantification of panel k (mean ± s.e.m., n = 3 experiments of 20 ROIs each, p-value < 0.0001, unpaired t-test).* ***m,*** *Tissue simulation recapitulates cell elimination after compression and rescue from elimination by depolarizing drugs (mean ± s.e.m., n=4 simulations).*

Depolarization rescues cells from elimination after mechanical compression

We wish to directly test the role of the membrane potential in regulating the response of cells to mechanical perturbations. Therefore, we grew MDCK cells on pre-stretched membranes to high cell number density and then decreased the stretch to induce cell crowding and compression of the tissue (Fig. 2k). Cell extrusion in response to tissue compression is well established[24,25]. If crowding induced hyperpolarization plays the central role cell in determining the cell number density, it should be possible to retain a higher cell number density simply by depolarizing the tissue. As we expected, in the presence of depolarizing drugs, cells maintained a significantly higher cell number density after the tissue was compressed (Fig. 2k,l red vs. cyan circles). The observed experimental dynamics are consistent with our model and could be recapitulated with the tissue simulation when we simulated uniaxial compression of the tissue (Fig. 2m). In a separate experiment, we induced crowding while cells were still in growth phase and observed the same increase of steady-state cell number density when cells were treated with a different depolarizing drug, TCT[16,17] (Fig. S8).

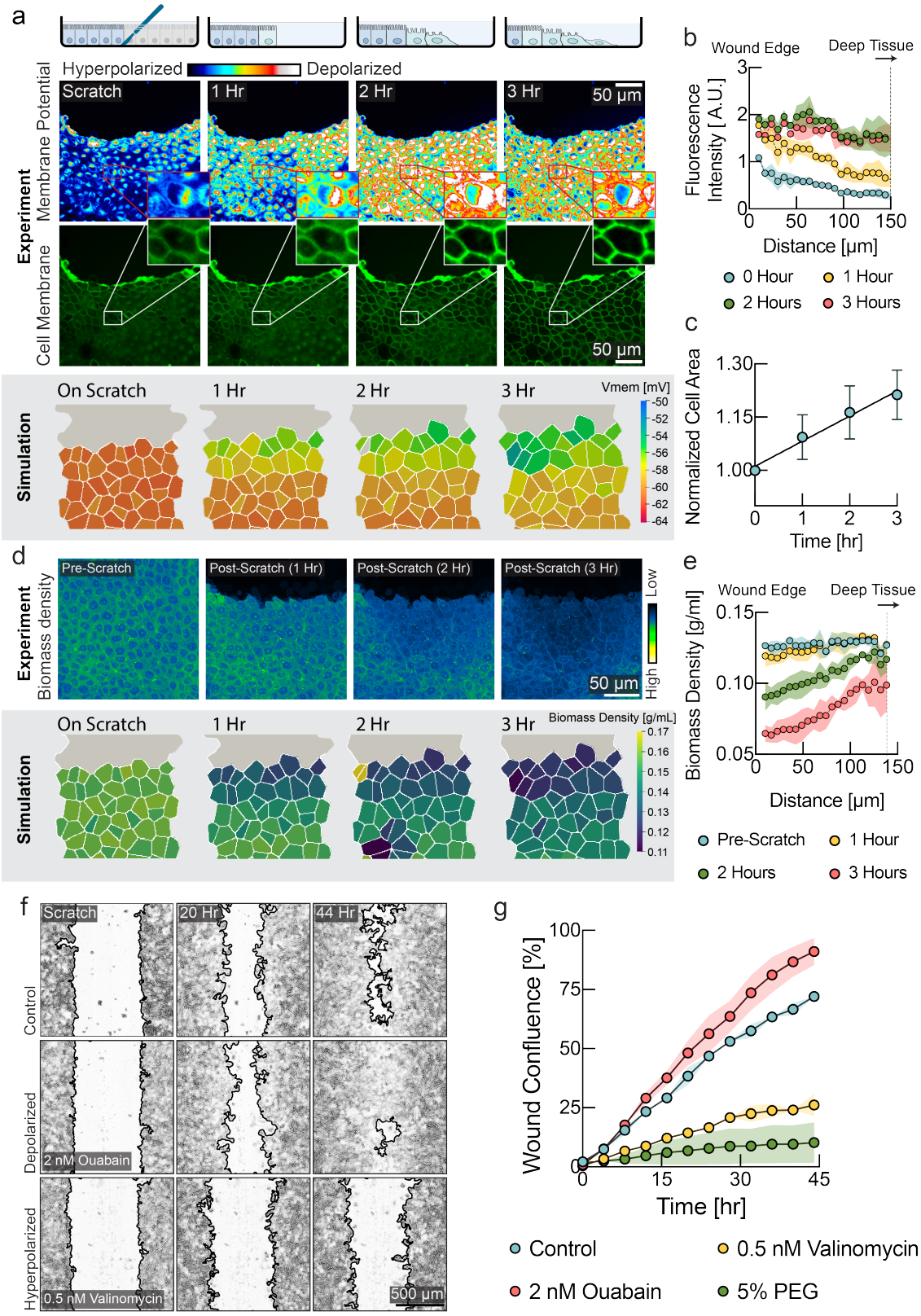
a
Hyperpolarized
Depolarized
Experiment
Membrane Potential
Cell Membrane
Scratch
1 Hr
2 Hr
3 Hr
50 µm
Simulation
On Scratch
Vmem [mV]
b
Wound Edge
Deep Tissue
Fluorescence Intensity [A.U.]
Distance [µm]
0 Hour
1 Hour
2 Hours
3 Hours
c
Normalized Cell Area
Time [hr]
d
Biomass density
Pre-Scratch
Post-Scratch (1 Hr)
Post-Scratch (2 Hr)
Post-Scratch (3 Hr)
Low
High
Biomass Density [g/mL]
e
Biomass Density [g/ml]
f
Control
Depolarized
Hyperpolarized
2 nM Ouabain
0.5 nM Valinomycin
500 µm
g
Wound Confluence [%]
Control
0.5 nM Valinomycin
2 nM Ouabain
5% PEG

Figure 3: A mechanically induced depolarization wave enhances wound healing. a, *Upper panel: DiSBAC$_2$(3) and fluorescently-labeled membrane images of MDCK cells imaged over 3 hours after scratch wound. A depolarization wave was observed from the wound edge up to several layers deep into the tissue. Lower panel: Membrane potential from the tissue simulation over the course of wound healing.* ***b****, Quantification of membrane potential as a function of distance from scratch wound at different times (mean ± s.d., n=4 rectangular ROIs of 100 µm width).* ***c,*** *Quantification of cell area shows expansion of cells during wound healing (mean ± s.d., n=9).* ***d,*** *Upper panel****:*** *NoRI images over the course of wound healing. Lower panel: Biomass density from the tissue simulation over the course of wound healing.* ***e.*** *Quantification of cellular biomass density as a function of distance from scratch wound at different times after wounding (mean ± s.d., n=4 rectangular ROIs of 50 µm width).* ***f,*** *Representative images of control, depolarizing drug treatment (ouabain) and hyperpolarizing drug treatment (valinomycin) during wound healing. Wound border outlines were generated using Wound healing size tool*[28]*.* ***g,*** *Quantification of wound area closure as a function of time (mean ± s.d., n=2 wells). Depolarization resulted in faster wound healing (ouabain, red circles), as compared to the untreated control (cyan circles). Hyperpolarization (valinomycin, yellow circles, 5% PEG, green circles) resulted in slower wound healing.*

Mechanical stretch results in a wave of depolarization during wound healing

Wound healing is a natural situation where substantial dynamical changes in tissue density and mechanical forces are occurring. All tissues can experience injuries that must be detected and quickly repaired in a controlled fashion. During wound healing, mechanisms of tissue homeostasis are operating in high gear and mechanical regulation may play an important role. To investigate the role of membrane potential in wound healing, we performed scratch wound assays on confluent MDCK monolayers. Strikingly, we observed a wave of depolarization in the tissue, starting at the wound's immediate edge and moving deeper into the tissue over several hours (Fig. 3a, quantified in 3b). Depolarization at wound edges has been previously observed, but the mechanistic cause of this depolarization has yet to be explained[29,30]. According to our model, a drop of biomass density due to mechanical stretching of the tissue could explain depolarization. Indeed, we observed an increase in cell area in the tissue indicative of mechanical stretch (Fig. 3a, middle & 3c), as cells became motile via epithelial mesenchymal transition (Fig. S9) and moved into the wound area, pulling on the cell behind them. Using NoRI imaging, we quantified biomass density as a function of distance from the wound edge (Fig. 3d, e & Fig. S10). Remarkably, we observed a drop in biomass density that closely coincided with the depolarization wave. Indeed, the tissue simulation with the mechano-electro-osmotic model successfully recapitulates the temporal and spatial dynamics of biomass density and membrane potential during wound healing (Fig. 3a, d, lower panels).

We hypothesize that the physiological function of this depolarization wave might be to upregulate motility forces and proliferation in cells that are not immediately adjacent to the wound edge. Based on the previous experiments, this would be expected to speed up the wound healing process. Indeed, we observed both depolarization (Fig. 3a) and a drop in biomass density (Fig. S9) in cells immediately adjacent to the wound, as they underwent the epithelial-mesenchymal transition. It is also known that motility forces of cells many cell rows away from the wound generate most of the tissue tension, resulting in wound closure[31]. Thus, according to this hypothesis, cells at the

immediate wound edge become motile first and move into the wound. The migration mechanically stretches cells in rows behind them. As this wave of mechanical stretch propagates deeper into the tissue, it causes a drop in biomass density, resulting in depolarization of membrane potential. Cells detecting the tissue stretching via the changed membrane potential may upregulate motility, biomass production and proliferation to enhance wound healing.

Depolarization enhances efficiency of wound healing

By applying depolarizing and hyperpolarizing drugs and quantifying wound healing speed, we tested whether modulation of the membrane potential directly affects the speed and efficiency of wound healing We used CHO cells instead of MDCK cells because MDCK tissues tended to detach entirely during scratch wounding when an automated scratch wounding device was used. Indeed, even low concentrations of hyperpolarizing drugs (valinomycin) dramatically slowed down wound healing (Fig. 3f, lower panel & Fig. 3g, yellow circles) as compared to the DMSO control. We had previously established that compression of cells by raising the external osmolarity resulted in hyperpolarization of membrane potential (Fig. S4). Indeed, compression by external osmolarity (Fig. 3g, green circles & Fig. S11) phenocopies the effect of hyperpolarizing drugs. Even more remarkably, we also found that the efficiency of wound healing could be increased, becoming faster than wild-type tissues with the addition of depolarizing drugs (Fig. 3f, middle & Fig. 3g, red circles). This is evident as compared to the untreated control (Fig.3f, upper & Fig. 3g, cyan circles). Depolarization by other drugs showed a similar improvement of wound healing efficiency (Fig. S11). These data suggest that depolarizing cells provides them with a 'head start' to upregulate motility and proliferation, as compared to the control tissue, where depolarization is only triggered later, by stretching from the other cells moving into the wound.

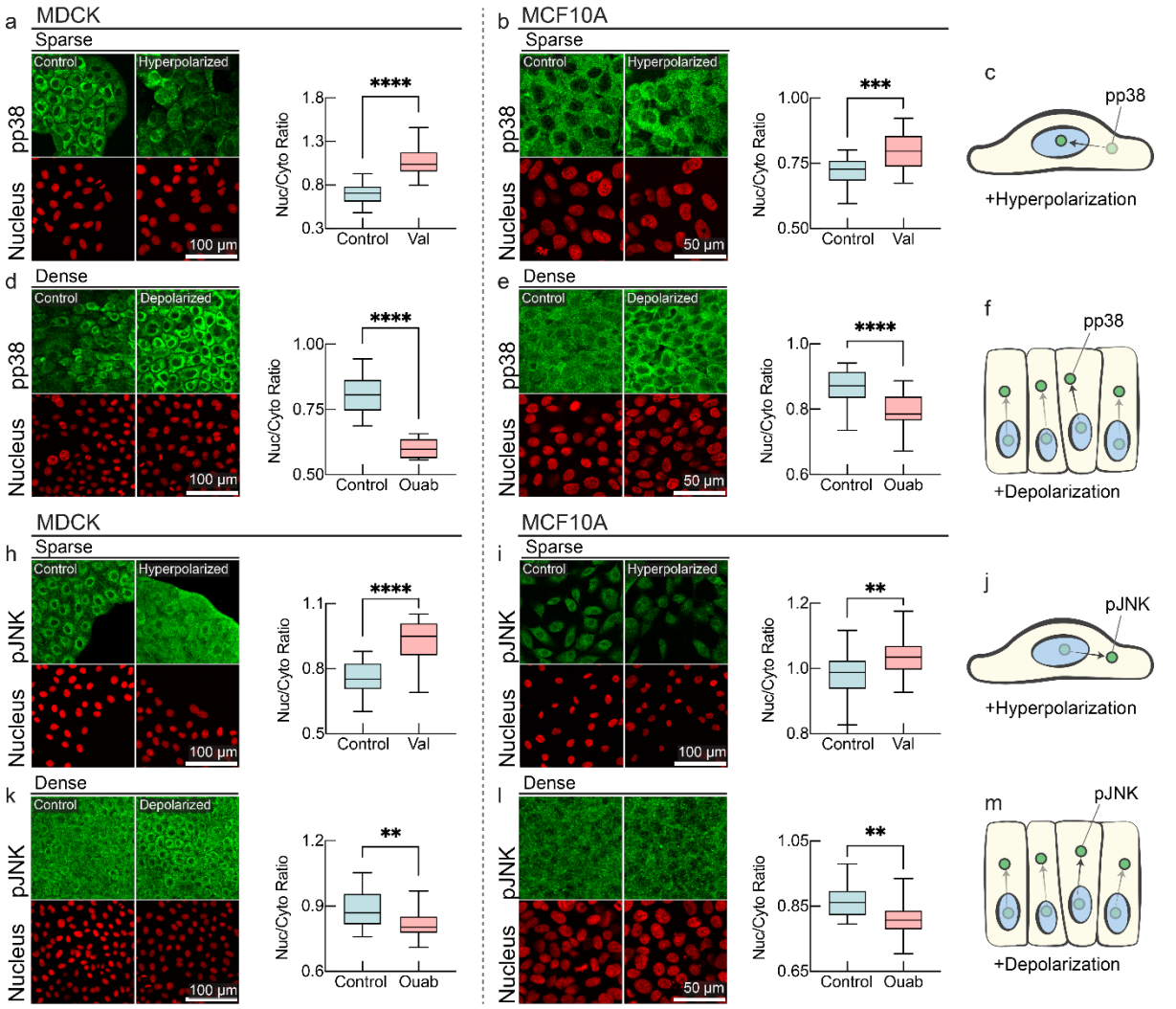

Figure 4: MAPK signaling is affected by membrane potential. a-f, *Membrane potential dependence of localization of phosphorylated p38 (pp38) in immunostaining. pp38 localizes predominantly in cytoplasm in sub-confluent (sparse) cells, and hyperpolarization by valinomycin results in augmented nuclear localization of pp38 in MDCK and MCF10 cells (panels a-b). pp38 localizes to cell nuclei in dense tissues, and Depolarization by ouabain results in nuclear exclusion of pp38 (panels c-d). Nuclear to cytoplasmic ratio of pp38 is quantified in accompanying plots (box plot, line at mean, error bars represent min to max, n=24, p-values: <0.0001 (MDCK sparse control vs valinomycin), <0.0001 (MDCK dense control vs ouabain), 0.0001 (MCF10A sparse control vs valinomycin), <0.0001 (MCF10A dense control vs ouabain)).* ***h-m,*** *Membrane potential dependence of localization of phosphorylated JNK in immunostaining. Nuclear to cytoplasmic ratio of pJNK is quantified in accompanying plots (box plot, line at mean, error bars represent min to max, n=24, p-values: <0.0001 (MDCK sparse control vs valinomycin), 0.003 (MDCK dense control vs ouabain), 0.0031 (MCF10A sparse control vs valinomycin), 0.0015 (MCF10A dense control vs ouabain)).*

Membrane potential controls MAPK signaling

Membrane potential appears to be a direct readout of mechanical forces and tissue density and plays an important role in tissue homeostasis, but how is it integrated with signal transduction pathways to mediate these phenotypes? We wondered whether membrane potential might directly affect pathways implicated in mechano-sensing such as the MAP Kinase (MAPK) pathway[8,32–37]. In a previous study, it was demonstrated that depolarization of the cellular membrane potential can induce K-Ras clustering, providing a plausible route to MAPK pathway activation, but its role on downstream effectors and pathway intermediates of MAPK signaling yet remained elusive. MAPK downstream effectors pp38 (p-Tyr 182) and pJNK (p-Thr 183, p-Tyr 185) have been previously indicated to be responsive to mechano-transduction, and we wanted to check if membrane potential can alter their cellular localization response[39–41]. In sub-confluent cells (hereby called sparse in contrast to fully confluent dense cells), pp38 and pJNK predominantly localize in the cytoplasm, whereas they predominantly localize in the nucleus in dense cells. Since sparse cells are more depolarized, we hypothesized that inducing hyperpolarization will cause pp38 and pJNK to translocate to the nucleus, mimicking a dense, hyperpolarized state (Fig 4c, j). In contrast, inducing depolarization in dense cells reverses this effect, causing pp38 and pJNK to become cytoplasmic (Fig 4f, m). Indeed, the addition of a hyperpolarizing drug (valinomycin, Fig. 4a-b, h-i) and a depolarizing drug (ouabain, Fig. 4d-e, k-l) caused pp38 and pJNK to exhibit this inversion effect in both MDCK and MCF10a cells. Mechanistically, nuclear localization of activated p38 and JNK at high tissue density may contribute to tissue homeostasis by suppressing proliferation, promoting autophagy, inducing apoptosis, or causing cell extrusion[38–40]. Reduction in the level of nuclear localized p-JNK under depolarization may promote proliferation at low tissue density.

Another important component of MAP kinase signaling pathway is the SRC kinase. We found that depolarization stabilized pSRC (Fig. S12a), while hyperpolarization strongly reduced its levels (Fig. S12a). Active SRC kinase signaling can activate many downstream targets, including EGFR[41–43] , PI3K[44], and PDK1, which can stimulate proliferation and motility. The downstream cellular responses elicited by membrane-potential-mediated SRC signaling are consistent with the role of membrane potential in tissue homeostasis and wound healing, shown in Figs. 1-3.

Membrane potential controls Hippo signaling

Our observations so far indicates that cellular membrane potential can be used as global readout for mechanical cues and membrane potential regulates pro and anti-proliferative pathways. The Hippo signaling pathway is another classically acclaimed mediator of mechano-transduction via the downstream effector YAP, which shuttles between nucleus and cytoplasm and promotes cell proliferation when localized to the nucleus[3,8].

Conventionally, the nuclear/cytoplasmic shuttling of YAP is thought to be akin to a step function [45], but we experimentally observed a continuous modulation of nuclear/cytoplasm ratio of YAP by cell number density (Fig. 5a-c). Next, we wanted to see if Hippo signaling can be modulated and overridden by altering the membrane potential. Strikingly, in both MDCK and MCF10a sparse cells, hyperpolarization causes significant nuclear exclusion and cytoplasmic localization of YAP (Fig. 5e,f upper panels) as compared to control. Previously, we reported that hyperpolarization causes lowering of the cell homeostatic density and negatively affects wound healing efficiency, which can be explained by anti-proliferative effect of nuclear exclusion of YAP under hyperpolarizing conditions. In dense cells, depolarization was also enough to induce YAP nuclear

reentry (Fig. 5e,f lower panels). Consistently, we also observed stabilization and increased level of total YAP levels under depolarizing conditions, whereas total YAP marginally decreased under hyperpolarization (Fig S12a). The observed regulation of YAP by membrane potential can easily be understood in the context of our physiological observations. Low tissue density results in depolarized membrane potential, resulting in localization of YAP to the nucleus, promoting cell growth and cell cycle progression[37,38]. On the other hand, high tissue density is reflected in hyperpolarized membrane potential, resulting in YAP exiting the nucleus and suppressing proliferation. Another previous observation[45] of nuclear reentry of YAP in confluent monolayer upon mechanical stretch can also be mechanistically explained by this work, as stretching causes a drop in biomass density and concomitant depolarization of cellular membrane potential (Fig. 2), and in its turn promotes nuclear re-entry of YAP.

pJNK and MST1 are intermediates in membrane potential-modulated Hippo signaling

Next, we wanted to elucidate the molecular mechanism by which changes in membrane potential leads to changes in YAP localization. Previous work has shown that pJNK-mediated LIMD1 phosphorylation inhibits LATS, which releases YAP from the LATS-YAP complex, promoting its nuclear translocation[46]. Since we have shown that pJNK is regulated by membrane potential, we wanted to check if pJNK plays a key role in controlling YAP localization under membrane potential perturbations. Experimentally, we took advantage of the twin cell lines EpH4-Ev and EpH4-1424, where the latter expresses constitutively active JNK. We added a JNK inhibitor (SP600125) to sparse EpH4-Ev cells (Fig. 5g) and observed significant nuclear exclusion of YAP. Additionally, JNK inhibition replicated this effect in sparse MDCK cells (Fig. S13a-b) and even caused YAP to become more cytoplasmic in dense MCF10A cells (Fig. S13 c-d).

If activated JNK is sufficient to drive YAP localization under depolarization, then the constitutively JNK-active EpH4-1424 cells should not respond to density-dependent YAP localization. However, we observed that YAP localization responded to cell number density changes, which suggests that while activated JNK is required for YAP nuclear localization (Fig. 5g, Fig. S13), it is not sufficient to regulate YAP localization.

Therefore, there must be other parallel routes of signal transduction of membrane potential in Hippo signaling. The canonical Hippo signaling pathway involves membrane localized receptor FAT1 and downstream signal transduction mediator MST1. Active MST1 phosphorylates LATS1/2, which in turn phosphorylates YAP to inhibit its nuclear localization. We hypothesized that if the FAT1-MST1 axis is involved in membrane potential signal transduction, then MST1 inhibition should break the transduction. To test this, we added a hyperpolarizing drug (valinomycin) to MDCK and MCF10A cells and observed nuclear exclusion of YAP (Fig. 5i,j). However, adding an MST1 inhibitor (XMU-MP-1) along with the hyperpolarizing drug reversed this effect and even caused YAP to become more nuclear (Fig. 5i, j). Therefore, the canonical Hippo signaling pathway with MST1 plays a role in membrane potential mediated signal transduction, but how exactly does the signal propagate from FAT1 to MST1 is still unclear.

Active MST1 is known to associate with the C-terminus tail of FAT1, a membrane receptor, and initiate multi-protein signalome assembly[47] in which it phosphorylates LATS1 to sequester YAP in the cytoplasm. Therefore, we hypothesized that FAT1 mediates the membrane potential signal

and generated a FAT1 KD MCF10a cell line. Using immunostaining, we observed that FAT1 is indeed localized on the cell membrane in sparse MCF10a cells, and the FAT1 signal disappeared in the knockdown cell line (Fig. 5k upper panel). Under hyperpolarization, we observe significant nuclear exclusion of YAP in the WT cell line, but YAP did not translocate to the nucleus in the knockdown cell line. This suggests that the FAT1-MST1 axis is critical in membrane potential mediated Hippo signal transduction.

How does FAT1 mediate membrane potential changes to signaling changes? Membrane potential can affect clustering of membrane leaflet associated signal transduction proteins like K-Ras and EGFR[48,49]. We hypothesized that membrane potential can affect the FAT1-MST1 complex assembly in a similar vein, which can in turn modulates downstream Hippo signaling. We observed that in sparse MDCK and MCF10a cells, MST1 is diffused in the cytoplasm, whereas in dense cells, MST1 organizes at the membrane (Fig. 5l), signifying its assembly with the c-terminus tail of FAT1. This inhibitory state is classically described as the 'Hippo-on' configuration that sequesters YAP in the cytoplasm. Strikingly, in sparse cells, hyperpolarization by valinomycin causes MST1 to form organized clusters on the membrane, mimicking the dense state (Fig. 5l left panel). In dense cells, depolarization by ouabain caused disruption of the membrane-organized distribution of MST1, making it become diffuse in the cytoplasm, turning off the inhibitory state and promoting YAP nuclear re-entry. Combining these results, we conclude that membrane potential mediated modulation of the Hippo signaling requires the FAT1-MST1 axis, and JNK-mediated route can further modulate signaling.

Decrease in biomass density and membrane potential in the beginning of *Xenopus* tail regeneration.

Using in-vitro tissue culture experiments, we have shown that during wound healing, a wave of membrane potential depolarization is concomitant with a wave of biomass density reduction, initiating from the wound edge into the tissue (Fig. 3). We wanted to test if a similar mechanism plays a role in in-vivo tissue as well. Using the xenopus embryo (stage 40) tail regeneration as a model system, we first validated that embryos regenerate tail properly after amputation (Fig. S14). We observed a gradient of depolarization from the wound edge and spanning over 6 cell layers 10 minutes after tail amputation (Fig. 6a-b). Using NoRI, we also observed a reduction in biomass density of the cells at the wound edge immediately after tail amputation (Fig. 6c left panels). After 10 minutes, we observed that, in most of the embryos, 5 to 6 layers of cells next to the wound edge dilute significantly (Fig. 6c right panels). This could be due to a rapid wound healing response where cell layers from the two lateral sides rapidly roll over and merge to seal the cut wound edge, thus inducing rapid dilution over a few cell layers within very short period.

We hypothesized that this biophysical coupling between biomass density and membrane potential is evolutionary conserved. To confirm this, we conducted a similar experiment with *Hydra vulgaris* and observed a similar gradient of biomass density dilution in epithelial and mesogleal cells after amputation of the body trunk (Fig. S15).

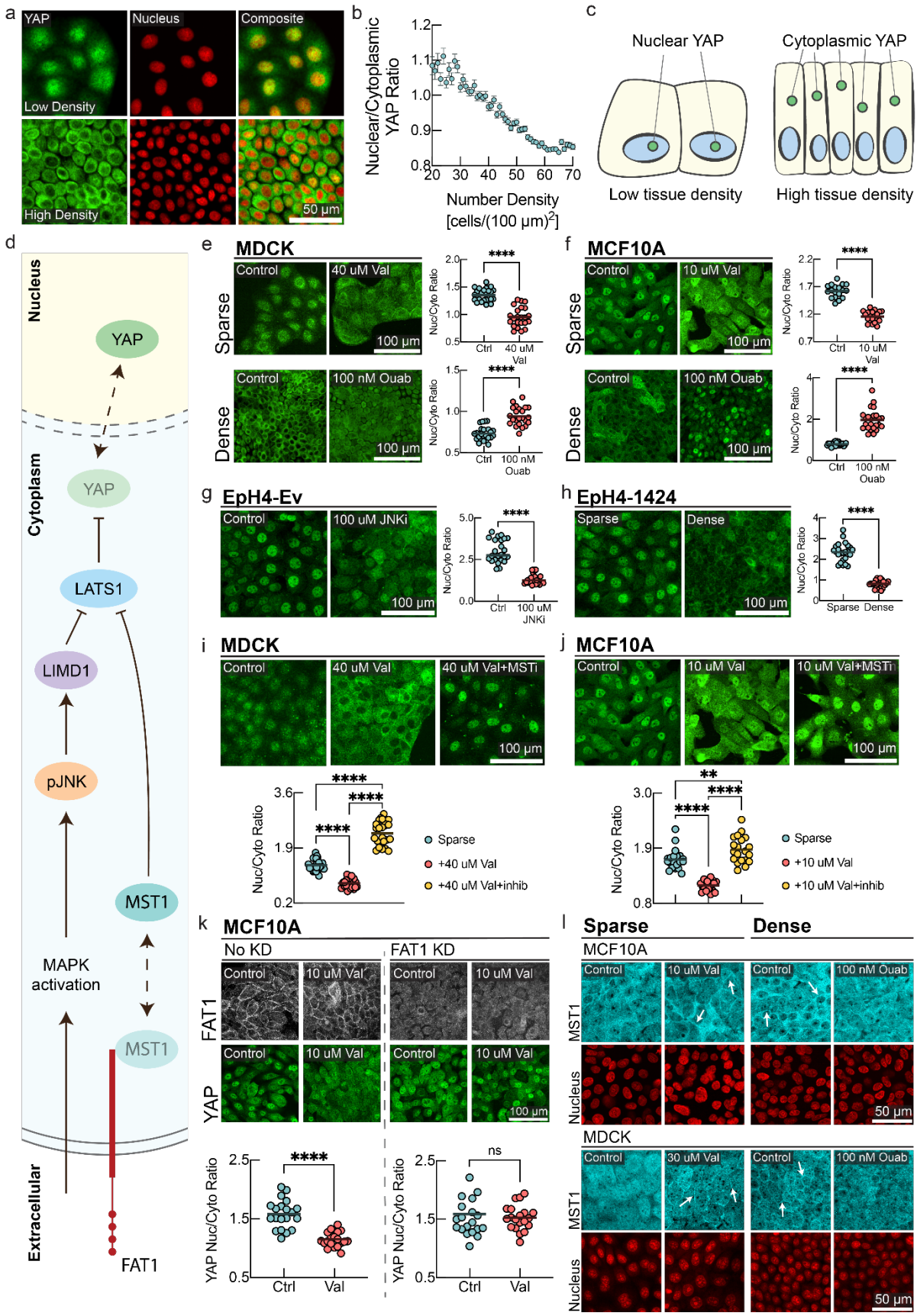
a
YAP
Nucleus
Composite
Low Density
High Density
50 µm
b
Nuclear/Cytoplasmic YAP Ratio
Number Density [cells/(100 µm)²]
c
Nuclear YAP
Cytoplasmic YAP
Low tissue density
High tissue density
d
Nucleus
YAP
Cytoplasm
YAP
LATS1
LIMD1
pJNK
MST1
MAPK activation
MST1
Extracellular
FAT1
e
MDCK
Sparse
Dense
Control
40 uM Val
100 nM Ouab
Nuc/Cyto Ratio
Ctrl
f
MCF10A
10 uM Val
g
EpH4-Ev
100 uM JNKi
h
EpH4-1424
Sparse
Dense
i
MDCK
40 uM Val+MSTi
+40 uM Val
+40 uM Val+inhib
j
MCF10A
10 uM Val+MSTi
+10 uM Val
+10 uM Val+inhib
k
MCF10A
No KD
FAT1 KD
FAT1
YAP
YAP Nuc/Cyto Ratio
Ctrl
Val
ns
l
Sparse
Dense
MCF10A
MST1
Nucleus
MDCK
30 uM Val
50 µm

Figure 5: Hippo signaling pathway is modulated by membrane potential. a, *YAP immunostaining and fluorescent nuclei images in low density (top panel) and high density MDCK monolayers (bottom panel).* ***b,*** *Quantification of nuclear/cytoplasmic YAP ratio as a function of cell number density. (mean ± s.d., n = 20337, cells binned together by local number density).* ***c,*** *Schematic representation of YAP localization at different cell number densities.* ***d,*** *Schematic diagram of different signaling intermediates in the Hippo pathway. MAPK activation promotes cytoplasmic pJNK, which activates LIMD1 to inhibit LATS1, causing YAP to translocate to the nucleus. In parallel, MST1 colocalizes with the c-terminus tail of FAT1. Release of MST1 from this complex inhibits LATS1 and causes YAP to translocate to the nucleus.* ***e-f****, YAP immunostaining of MDCK/MCF10A cells under sparse (top panels) and dense (bottom panels) conditions with corresponding drug perturbations.* ***g****, YAP immunostaining of sparse EpH4-Ev cells under control and JNK inhibitor (SP600125) conditions.* ***h****, YAP immunostaining of sparse and dense EpH4-1424 cells with quantification.* ***i-j****, YAP immunostaining of sparse MDCK/MCF10A cells with control, valinomycin, and valinomycin with MST inhibitor (XMU-MP-1) conditions. The p-value between sparse and valinomycin+MSTi conditions is 0.0092.* ***k****, Sparse MCF10A cells with and without FAT1 knockdown (KD) are stained for FAT1 and YAP under control and valinomycin conditions. The nucleus/cytoplasm ratio for FAT1KD cells under control vs valinomycin has a p-value of 0.558 (ns).* ***l****, MST1 immunostaining of MCF10A/MDCK cells under sparse control, sparse valinomycin, dense control, and dense ouabain conditions. White arrows highlight areas of increased MST1 organized membrane clusters. For quantifications in panels* ***e-k****, the nucleus/cytoplasm ratio of YAP is measured. In the plots, the line is at mean, n=24, and p-value is measured with an unpaired t-test and is <0.0001 unless otherwise specified,*

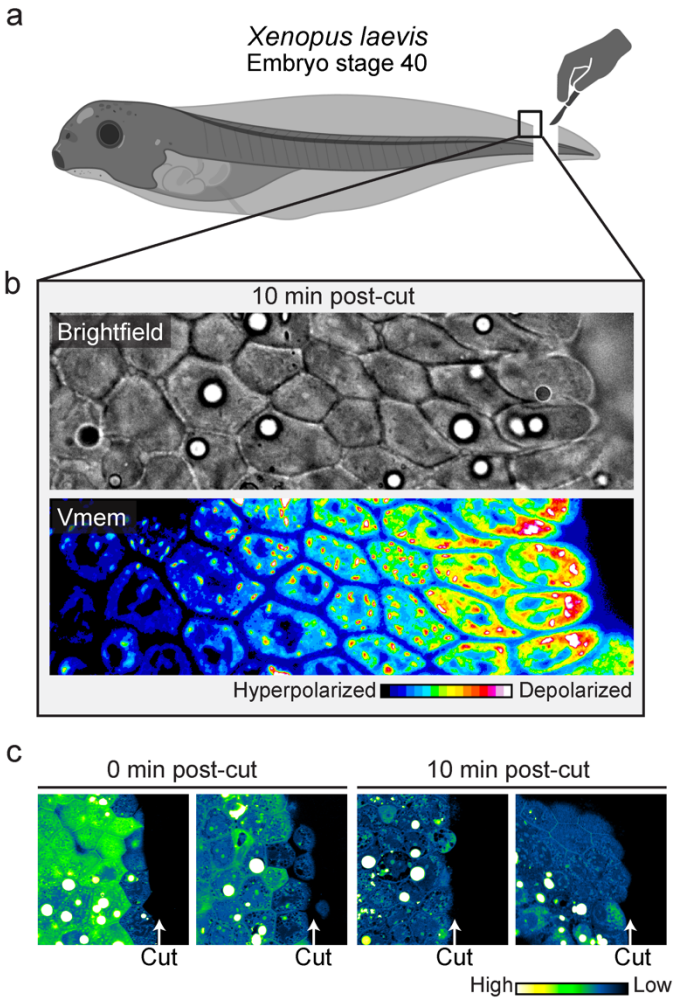

Figure 6: ***Interplay of membrane potential and cytoplasmic density dilution happens at the beginning of Xenopus tail regeneration. a****, Schematic diagram showing the experimental set up for xenopus embryo tail amputation.* ***b****, Brightfield and membrane potential (DiSBAC$_2$(3)) images of xenopus wound edge 10 minutes post-amputation. Cell layers get progressively depolarized from deep tissue to the wound edge.* ***c****, NoRI images of xenopus tail amputation 0 min and 10 min post-cut. One cell layer becomes dilute in biomass density immediately after the cut, and 5-6 cell layers become dilute in 10 minutes. Images represent different xenopus embryos amputated and fixed after the specified amount of time.*

Discussion

Regulation by membrane potential can convey the size, density, and the general mechanical state of a cell. These global cellular variables are of central physiological importance for homeostasis and development, but such cell-scale properties are difficult for cells to accurately assess from local protein interactions, such as cell-cell adhesion or even stretch-activated ion channels in the plasma membrane. Membrane potential on the other hand, provides a quasi-instantaneous, globally integrated readout of cell state. The coupling between mechanical pressure, density and membrane potential is based only on elementary physical laws, requires no active regulation, and is present even in thermodynamic equilibrium, where it is known as the Gibbs-Donnan effect [13]. Therefore,

even primitive cells, lacking active transport and confined by a simple cell wall, could have utilized membrane potential as a readout of their mechanical state and biomass concentration. Membrane-potential-mediated mechano-transduction may therefore have been among the first homeostatic mechanisms to emerge in multicellular organisms.

Note that while we assumed the absence of active regulation or amplification of membrane potential in our model as a proof-of-concept, there are many ways how cells could further enhance the changes in membrane potential to reflect even small differences in density and mechanical forces. We believe it is likely that rather than fixing membrane potential to a constant homeostatic value (like body temperature in mammals), which would result in a loss of the valuable information conveyed by membrane potential, cells may have evolved to actively enhance the signal-to-noise ratio of membrane potential signaling of mechanical pressure. Indeed, observed changes in membrane potential are sometimes even larger than those expected from our model without signal amplification (Fig. S3).

Note also that while we have shown that several important mechano-transduction pathways are controlled by membrane potential, there are likely other parallel signal transduction routes that are affected by membrane potential. Calcium signaling would be an ideal effector of membrane-potential-mediated mechano-transduction. This could occur either via voltage-gated channels in the plasma membrane and the strong voltage-dependence of equilibrium calcium concentration that results from the calcium ion's two positive charges. Indeed, flux through key calcium channels like Piezo has been shown to strongly depend on membrane potential[50] and Piezo has been shown to be voltage-gated[51].

The concept of mechano-sensing via membrane potential should not be thought of as limited to epithelia or even multi-cellular tissues. For instance, stem cell differentiation has been shown to depend on both cell volume and osmotic pressure[52,53], as well as membrane potential[54], suggesting a role of membrane-potential-mediated mechanical signaling. As another example, the response of membrane potential to cellular compression may play a role in neuronal mechano-transduction if mechanical forces affect total neuronal cell volume. The resulting changes in resting membrane potential could trigger voltage-gated channels and calcium siganling[50,51].

Finally, the importance of membrane potential in tissue growth control that we observe, suggests that mis-regulation of membrane potential or its downstream signaling cascade could have dramatic consequences for tissue homeostasis, potentially resulting in tumorigenesis when cells stop responding to the mechanical cues from their environment. In fact, this may explain the frequent occurrence of ectopic expression of neuronal ion channels in tumors[55] and the commonly observed phenotype of depolarized resting membrane potential in cancer[56].

Acknowledgements
We would like to thank Sean Megason, Tim Mitchison, Jan Skotheim, and Xavier Trepat for their comments and feedback on the manuscript. We would like to thank Peter Sorger and Clarance Yapp for access to their high content imaging systems. Thanks to Eugenia Piddini (University of Bristol), J.J. Fredberg and C.Y. Park (Harvard T.H. Chan School of Public Health) for helping us with MDCK cells. We thank Nikon imaging center at Harvard Medical School for help with all fluorescence imaging experiments. Specifically, we thank Jennifer Waters, Tally Lambert, Anna

Payne-Tobin Jost for their valuable support with the microscopy.Thanks to Florian Engert for helping us with Hydra experiments, and special thanks to Andrew Murphy of Sean Megason lab for helping us with Hydra husbandry. Thanks to Bill Jia of Megason lab for valuable comments on membrane potential measurement. This project was supported by MIRA grant (5R35GM137895) and an HMS Junior Faculty Armenise grant to M.B. N.C.B was supported by following grants National Science Foundation Graduate Research Fellowship Program (DGE 2140743) and Systems, Synthetic, and Quantitative Biology Training grant award (T32GM135014). YH was supported by HCRP of Harvard College. Any opinions, findings, and conclusions or recommendations expressed in this material are those of the author(s) and do not necessarily reflect the views of the National Science Foundation.

References

1. *Molecular Biology of the Cell: Reference Edition, Band 1*. (2008).
2. Hille, B. Ion channels of excitable membranes. in (2001).
3. Panciera, T., Azzolin, L., Cordenonsi, M. & Piccolo, S. Mechanobiology of YAP and TAZ in physiology and disease. *Nat Rev Mol Cell Biol* **18**, 758–770 (2017).
4. Niisato, N., Post, M., Van Driessche, W. & Marunaka, Y. Cell Swelling Activates Stress-Activated Protein Kinases, p38 MAP Kinase and JNK, in Renal Epithelial A6 Cells. *Biochem Biophys Res Commun* **266**, 547–550 (1999).
5. Kishi, H. *et al.* Osmotic Shock Induces G1 Arrest through p53 Phosphorylation at Ser33 by Activated p38MAPK without Phosphorylation at Ser15 and Ser20. *Journal of Biological Chemistry* **276**, 39115–39122 (2001).
6. Lee, S.-H., Park, Y., Yoon, S. K. & Yoon, J.-B. Osmotic Stress Inhibits Proteasome by p38 MAPK-dependent Phosphorylation. *Journal of Biological Chemistry* **285**, 41280–41289 (2010).
7. HuangFu, W.-C., Omori, E., Akira, S., Matsumoto, K. & Ninomiya-Tsuji, J. Osmotic Stress Activates the TAK1-JNK Pathway While Blocking TAK1-mediated NF-κB Activation. *Journal of Biological Chemistry* **281**, 28802–28810 (2006).
8. Dupont, S. *et al.* Role of YAP/TAZ in mechanotransduction. *Nature* **474**, 179–183 (2011).
9. Buckley, C. E. & St Johnston, D. Apical–basal polarity and the control of epithelial form and function. *Nat Rev Mol Cell Biol* **23**, 559–577 (2022).
10. Oh, S. *et al.* Protein and lipid mass concentration measurement in tissues by stimulated Raman scattering microscopy. *Proc Natl Acad Sci U S A* **119**, e2117938119 (2022).
11. Park, H. *et al.* Three-dimensional refractive index tomograms and deformability of individual human red blood cells from cord blood of newborn infants and maternal blood. *https://doi.org/10.1117/1.JBO.20.11.111208* **20**, 111208 (2015).
12. Shin, S., Kim, K., Yoon, J. & Park, Y. Active illumination using a digital micromirror device for quantitative phase imaging. *Optics Letters, Vol. 40, Issue 22, pp. 5407-5410* **40**, 5407–5410 (2015).
13. Donnan, F. G. Theorie der Membrangleichgewichte und Membranpotentiale bei Vorhandensein von nicht dialysierenden Elektrolyten. Ein Beitrag zur physikalisch-

chemischen Physiologie. *Zeitschrift für Elektrochemie und angewandte physikalische Chemie* **17**, 572–581 (1911).
14. Abdelfattah, A. S. *et al.* Bright and photostable chemigenetic indicators for extended in vivo voltage imaging. *Science (1979)* **365**, 699–704 (2019).
15. Cone, C. D. & Tongier, M. Contact inhibition of division: involvement of the electrical transmembrane potential. *J Cell Physiol* **82**, 373–86 (1973).
16. Barboiu, M. *et al.* Polarized Water Wires under Confinement in Chiral Channels. *J Phys Chem B* **119**, 8707–8717 (2015).
17. Barboiu, M. *et al.* An artificial primitive mimic of the Gramicidin-A channel. *Nat Commun* **5**, 4142 (2014).
18. Goldman, D. E. POTENTIAL, IMPEDANCE, AND RECTIFICATION IN MEMBRANES. *J Gen Physiol* **27**, 37 (1943).
19. TOSTESON, D. C. & HOFFMAN, J. F. Regulation of Cell Volume by Active Cation Transport in High and Low Potassium Sheep Red Cells. *Journal of General Physiology* **44**, 169–194 (1960).
20. Kay, A. R. & Blaustein, M. P. Evolution of our understanding of cell volume regulation by the pump-leak mechanism. *Journal of General Physiology* **151**, 407–416 (2019).
21. Armstrong, C. M. The Na/K pump, Cl ion, and osmotic stabilization of cells. *Proceedings of the National Academy of Sciences* **100**, 6257–6262 (2003).
22. Dyer, K. F. The Quiet Revolution: A New Synthesis of Biological Knowledge. *J Biol Educ* **5**, 15–24 (1971).
23. Milo, R., Jorgensen, P., Moran, U., Weber, G. & Springer, M. BioNumbers—the database of key numbers in molecular and cell biology. *Nucleic Acids Res* **38**, D750 (2010).
24. Eisenhoffer, G. T. & Rosenblatt, J. Bringing balance by force: live cell extrusion controls epithelial cell numbers. *Trends Cell Biol* **23**, 185–192 (2013).
25. Eisenhoffer, G. T. *et al.* Crowding induces live cell extrusion to maintain homeostatic cell numbers in epithelia. *Nature* **484**, 546–549 (2012).
26. Park, J. *et al.* Screening fluorescent voltage indicators with spontaneously spiking HEK cells. *PLoS One* **8**, (2013).
27. Burgstahler, R. *et al.* Confocal ratiometric voltage imaging of cultured human keratinocytes reveals layer-specific responses to ATP. *Am J Physiol Cell Physiol* **284**, (2003).
28. Suarez-Arnedo, A. *et al.* An image J plugin for the high throughput image analysis of in vitro scratch wound healing assays. *PLoS One* **15**, e0232565 (2020).
29. Chifflet, S. *et al.* Early and late calcium waves during wound healing in corneal endothelial cells. *Wound Repair and Regeneration* **20**, 28–37 (2012).
30. Reid, B. & Zhao, M. The Electrical Response to Injury: Molecular Mechanisms and Wound Healing. *Adv Wound Care (New Rochelle)* **3**, 184–201 (2014).
31. Trepat, X. *et al.* Physical forces during collective cell migration. *Nat Phys* **5**, 426–430 (2009).
32. Chang, Y. C., Wu, J. W., Wang, C. W. & Jang, A. C. C. Hippo Signaling-Mediated Mechanotransduction in Cell Movement and Cancer Metastasis. *Front Mol Biosci* **6**, 157 (2020).

33. HuangFu, W.-C., Omori, E., Akira, S., Matsumoto, K. & Ninomiya-Tsuji, J. Osmotic Stress Activates the TAK1-JNK Pathway While Blocking TAK1-mediated NF- B Activation: TAO2 REGULATES TAK1 PATHWAYS. *Journal of Biological Chemistry* **281**, 28802–28810 (2006).
34. Lee, S.-H., Park, Y., Yoon, S. K. & Yoon, J.-B. Osmotic stress inhibits proteasome by p38 MAPK-dependent phosphorylation. *J Biol Chem* **285**, 41280–9 (2010).
35. Kishi, H. *et al.* Osmotic shock induces G1 arrest through p53 phosphorylation at Ser33 by activated p38MAPK without phosphorylation at Ser15 and Ser20. *J Biol Chem* **276**, 39115–22 (2001).
36. Messaoud, N. ben, Katzarova, I. & López, J. M. Basic Properties of the p38 Signaling Pathway in Response to Hyperosmotic Shock. doi:10.1371/journal.pone.0135249.
37. Niisato, N., Post, M., van Driessche, W. & Marunaka, Y. Cell Swelling Activates Stress-Activated Protein Kinases, p38 MAP Kinase and JNK, in Renal Epithelial A6 Cells. *Biochem Biophys Res Commun* **266**, 547–550 (1999).
38. Zeke, A., Misheva, M., Reményi, A. & Bogoyevitch, M. A. JNK Signaling: Regulation and Functions Based on Complex Protein-Protein Partnerships. *Microbiol Mol Biol Rev* **80**, 793 (2016).
39. Maik-Rachline, G., Lifshits, L. & Seger, R. Nuclear P38: Roles in Physiological and Pathological Processes and Regulation of Nuclear Translocation. *International Journal of Molecular Sciences 2020, Vol. 21, Page 6102* **21**, 6102 (2020).
40. Dhanasekaran, D. N. & Reddy, E. P. JNK signaling in apoptosis. *Oncogene* **27**, 6245–6251 (2008).
41. Stover, D. R., Becker, M., Liebetanz, J. & Lydon, N. B. Src Phosphorylation of the Epidermal Growth Factor Receptor at Novel Sites Mediates Receptor Interaction with Src and P85α. *Journal of Biological Chemistry* **270**, 15591–15597 (1995).
42. Tice, D. A., Biscardi, J. S., Nickles, A. L. & Parsons, S. J. Mechanism of biological synergy between cellular Src and epidermal growth factor receptor. *Proceedings of the National Academy of Sciences* **96**, 1415–1420 (1999).
43. Maa, M. C., Leu, T. H., McCarley, D. J., Schatzman, R. C. & Parsons, S. J. Potentiation of epidermal growth factor receptor-mediated oncogenesis by c-Src: implications for the etiology of multiple human cancers. *Proceedings of the National Academy of Sciences* **92**, 6981–6985 (1995).
44. Beadnell, T. C. *et al.* Src-mediated regulation of the PI3K pathway in advanced papillary and anaplastic thyroid cancer. *Oncogenesis* **7**, 23 (2018).
45. Benham-Pyle, B. W., Pruitt, B. L. & Nelson, W. J. Mechanical strain induces E-cadherin–dependent Yap1 and β-catenin activation to drive cell cycle entry. *Science (1979)* **348**, 1024–1027 (2015).
46. Codelia, V. A., Sun, G. & Irvine, K. D. Regulation of YAP by Mechanical Strain through Jnk and Hippo Signaling. *Current Biology* **24**, 2012–2017 (2014).
47. Martin, D. *et al.* Assembly and activation of the Hippo signalome by FAT1 tumor suppressor. *Nat Commun* **9**, 2372 (2018).
48. Wang, Y. *et al.* Regulation of EGFR nanocluster formation by ionic protein-lipid interaction. *Cell Res* **24**, 959–976 (2014).
49. Zhou, Y. *et al.* Membrane potential modulates plasma membrane phospholipid dynamics and K-Ras signaling. *Science (1979)* **349**, 873–876 (2015).

50. Coste, B. *et al.* Piezo1 and Piezo2 are essential components of distinct mechanically activated cation channels. *Science (1979)* **330**, 55–60 (2010).
51. Moroni, M., Servin-Vences, M. R., Fleischer, R., Sánchez-Carranza, O. & Lewin, G. R. Voltage gating of mechanosensitive PIEZO channels. *Nature Communications 2018 9:1* **9**, 1–15 (2018).
52. Guo, M. *et al.* Cell volume change through water efflux impacts cell stiffness and stem cell fate. *Proc Natl Acad Sci U S A* **114**, E8618–E8627 (2017).
53. Fan, Y. L., Zhao, H. C. & Feng, X. Q. Hypertonic pressure affects the pluripotency and self-renewal of mouse embryonic stem cells. *Stem Cell Res* **56**, 102537 (2021).
54. Levin, M. Leading Edge Bioelectric signaling: Reprogrammable circuits underlying embryogenesis, regeneration, and cancer. *Cell* **184**, 1971–1989 (2021).
55. Li, M. & Xiong, Z. G. Ion channels as targets for cancer therapy. *Int J Physiol Pathophysiol Pharmacol* **3**, 156 (2011).
56. Yang, M. & Brackenbury, W. J. Membrane potential and cancer progression. *Front Physiol* **4**, (2013).